Identification of Buried Unexploded Ordnance From Broadband Electromagnetic Induction Data

Stephen J. Norton and I. J. Won

***Abstract*— A procedure is described for computing range and orientation invariant spectral signatures of buried unexploded ordnance (UXO) from electromagnetic induction (EMI) data. The normalized eigenvalues of the magnetic polarizability tensor that characterizes the target response are used as the orientation-invariant spectral signatures. It is shown that the eigenvalues can be normalized with respect to depth under the assumption that a multiplicative scale factor can be applied at all frequencies. The eigenvalues are derived by measuring the matrix elements of the polarizability tensor from above-ground spatial data and then by diagonalizing this matrix. This method is linear, and does not require a nonlinear parameter search. After normalizing for depth, the eigenvalues derived from an unknown object can then be compared with library eigenvalues using the L2 norm as a goodness-of-fit measure. The procedure is demonstrated using data obtained from cylinders and UXO at different orientations.**

I. Introduction

GEOPHEX, Ltd., has developed a series of multifrequency electromagnetic induction (EMI) sensors [1]–[3] for detecting and characterizing buried conducting anomalies. These sensors have recently been shown to be effective in detecting and identifying buried unexploded ordnance (UXO). The Geophex GEM-3 sensor, which uses coaxial transmit and receive coils, is particularly well suited for this purpose because of its multifrequency capability and its compact spatial footprint [2]. This instrument also employs a unique transmit-bucking scheme to null the primary field at the location of the receiving coil. In the current work, the GEM-3 sensor was used over a frequency range of 30 Hz to 20 kHz. This range of frequencies is in the quasistatic regime, in which propagation effects are negligible and induction effects predominate.

Other researchers have used EMI data in an attempt to identify buried UXO. One approach is based on an algorithm that performs a fit to a dipole model using EMI data recorded at multiple points on the surface [4], [5]. Typically, the target is assumed to have axial symmetry. The dipole-fitting algorithm then performs a nonlinear search for a set of parameters that describe the target, for example, the x, y, and z coordinates of its centroid, two angles defining its orientation, and two eigenvalues characterizing its longitudinal and transverse responses. A related technique has been independently proposed for the purpose of landmine identification [6].

Manuscript received July 5, 2000; revised April 13, 2001. This work was supported in part by the Department of Defense Environmental Security Technology Certification Program (ESTCP) and by U.S. Army Phase II SBIR Contract DACA3999-C-001, Engineering Research and Development Center (ERDC).

The authors are with Geophex, Ltd., Raleigh, NC 27603 USA (e-mail: norton@geophex.com).

Publisher Item Identifier S 0196-2892(01)08835-0.

Here we describe an approach that has the same objective of identifying unknown UXO but is linear and noniterative. This has several potential advantages over nonlinear search schemes: 1) the method is computationally fast, requiring a single linear least-squares inversion followed by an eigendecomposition of a 3×3 matrix; 2) the method avoids pitfalls associated with iterative, nonlinear algorithms, such as sensitivity to starting values and the possibility of getting trapped in local minima, and 3) a sensitivity analysis can be conveniently performed using the singular-value decomposition to assess the "observability" of the matrix elements of the polarizability tensor for a given set of measurement positions. Here the term "observability" refers to how well a particular matrix element can be resolved by a set of spatial measurements. This is discussed further below.

An effective methodology for identifying UXO is to record first a set of "library spectra" derived from known UXO types over a broad spectral range. Identification of an unknown target can then be performed by comparing spectral data acquired from the target to the set of library spectra. However, a direct comparison between the raw sensor data and the library data is not feasible because the UXO spectrum varies with its orientation and distance from the sensor head. As a result, a preprocessing step is needed to extract invariant target signatures from the raw data that are independent of range and orientation. These invariant signatures can then be compared to similarly-derived library signatures to identify the type of UXO, or to identify the target as clutter. We describe below a procedure for deriving such signatures.

II. Theory

From reciprocity principles, the response of the sensor can be expressed in the following general form [7]–[9]:

$$emf_R = \boldsymbol{H}_T \cdot \boldsymbol{P} \cdot \boldsymbol{H}_R \tag{1}$$

where emf_R is the emf induced in the receiving coil. Here $\boldsymbol{H}_T$ is the incident magnetic field at the location of the target (i.e., the field in the absence of the target) generated by the transmitting coil. Similarly, $\boldsymbol{H}_R$ is the incident field generated by the receiving coil if it were used as a transmitter. In (1), the target is characterized by $\boldsymbol{P}$, which is a 3×3 complex, symmetric matrix known as the magnetic polarizability tensor. If the skin depth in the earth in which the target is embedded is long compared to the target depth, then the fields $\boldsymbol{H}_T$ and $\boldsymbol{H}_R$ may be regarded as frequency independent and the frequency response of the target is contained in the tensor $\boldsymbol{P}$ only. This should be valid for real earth conductivities (under 1 S/m), typical EMI

frequencies (under 100 kHz), and typical UXO depths (0 to 2 m).

Equation (1) can be identified as the first term in a multipole expansion of the target response in which the higher order terms have been neglected. If the coils are regarded as dipoles, this term may be written approximately as

$$emf_R = \frac{c}{r_T^3 r_R^3} \boldsymbol{n}_T \cdot \boldsymbol{P} \cdot \boldsymbol{n}_R \tag{2}$$

where

c	constant independent of range and frequency;
$\boldsymbol{n}_T$ and $\boldsymbol{n}_R$	unit vectors in the directions of the incident fields $\boldsymbol{H}_T$;
$\boldsymbol{H}_R$, and r_T and r_R	distances from the target to the transmit and receiver coils.

For a monostatic system, $r = r_T = r_R$ and $\boldsymbol{n}_T = \boldsymbol{n}_R = \boldsymbol{n}$, so (2) reduces to

$$emf_R = \frac{c}{r^6} \boldsymbol{n} \cdot \boldsymbol{P} \cdot \boldsymbol{n}. \tag{3}$$

The second term in the multipole expansion is smaller than the lowest-order term, given by (3), by a factor of about $(d/r)^2$, where d is the characteristic dimension of the target. The neglected terms in the expansion fall off as r^{-8}, r^{-10}, and so on. Thus, the approximation expressed by (1) is expected to be reasonable at target ranges three or four times the target size or greater.

In view of (3), one could attempt to remove the range dependence by scaling the data by a factor of r^{-6}. This approach is prone to error for several reasons. First, r would need to be accurately estimated by some independent means (e.g., employing magnetometry data) or by a dipole fitting procedure of some kind. However, the rate of change of r^{-6} is large, so a small error in the target location will lead to a large error in r^{-6}. Moreover, the dipole approximation for the transmit and receive loops is not accurate for nearby targets, and the range dependence for finite loop sizes is considerably more complex than r^{-6}. We thus consider a more general approach that assumes an arbitrary range dependence $f(r)$ derivable from the data.

Let us rewrite (3) in the form

$$emf_R = \boldsymbol{n} \cdot \boldsymbol{S} \cdot \boldsymbol{n} \tag{4}$$

where we define the modified polarizability tensor

$$\boldsymbol{S} = f(r)\boldsymbol{P} \tag{5}$$

and $f(r)$ is an unknown range-dependent scale factor. We require that $f(r)$ depend only on r and not on frequency. A procedure for estimating $f(r)$ is given below. We now describe a methodology for generating range and orientation invariant target signatures from data acquired using the GEM-3 sensor.

III. Orientation Invariants

We propose using the eigenvalues of the modified polarizability matrix $\boldsymbol{S}$ in (4) as our orientation-invariant spectral signatures. Our procedure is to measure the matrix elements of $\boldsymbol{S}$ from data recorded at multiple positions on the surface. Diagonalizing $\boldsymbol{S}$ then gives its eigenvalues and eigenvectors, where the latter define the principal axes of the target and hence its orientation. The eigenvalues are an intrinsic property of the target and depend on its size, shape, and composition, but do not depend on its orientation. For a uniform ellipsoidal object, the eigenvalues can be related to the lengths of the semi-major axes of the ellipsoid. Reference [7] gives explicit formulas for the case of a spheroidal target. In the latter case, due to axial symmetry, two of the eigenvalues coincide, which correspond to the two transverse directions of the spheroid.

TABLE I
Cylinder Data

1.	Aluminum cylinder	Vertical	Free space
2.	Aluminum cylinder	Horizontal	Free space
3.	Aluminum cylinder	45 Degrees	Free space
4.	Aluminum cylinder	Vertical	In ground
5.	Aluminum cylinder	Horizontal	In ground
6.	Aluminum cylinder	45 Degrees	In ground
7.	Brass cylinder	Vertical	Free space
8.	Brass cylinder	Horizontal	Free space
9.	Brass cylinder	45 Degrees	Free space
10.	Brass cylinder	Vertical	In ground
11.	Brass cylinder	Horizontal	In ground
12.	Brass cylinder	45 Degrees	In ground
13.	Steel cylinder	Vertical	Free space
14.	Steel cylinder	Horizontal	Free space
15.	Steel cylinder	45 Degrees	Free space
16.	Steel cylinder	Vertical	In ground
17.	Steel cylinder	Horizontal	In ground
18.	Steel cylinder	45 Degrees	In ground

In measuring the matrix elements of $\boldsymbol{S}$, the first step is to estimate the direction of the incident field at the target location, denoted by the unit vector $\boldsymbol{n}$. In principle, this requires knowledge of the target location relative to the sensor head; we can then compute the incident field $\boldsymbol{H}$ at the target, from which $\boldsymbol{n} = \boldsymbol{H}/|\boldsymbol{H}|$. The target location (its depth and transverse coordinates) can be estimated, for example, by fitting the target response to a dipole model using either EMI or magnetometry data. Alternatively, an approximate estimate of the target's transverse coordinates can be obtained from the peak of the surface anomaly, and an estimate of its depth can be derived from the half-width of the surface anomaly. We note that, although the amplitude of the field is very depth sensitive, the field direction, denoted by $\boldsymbol{n}$, is less so. Thus, some uncertainty in the target location for the purpose of computing $\boldsymbol{n}$ is probably tolerable; so far, this has been borne out by our experience. Uncertainties in amplitude are treated using the depth scaling procedure to be described.

Once the unit vector $\boldsymbol{n}$ has been computed for each sensor position, we obtain the matrix elements of $\boldsymbol{S}$ from the spatially

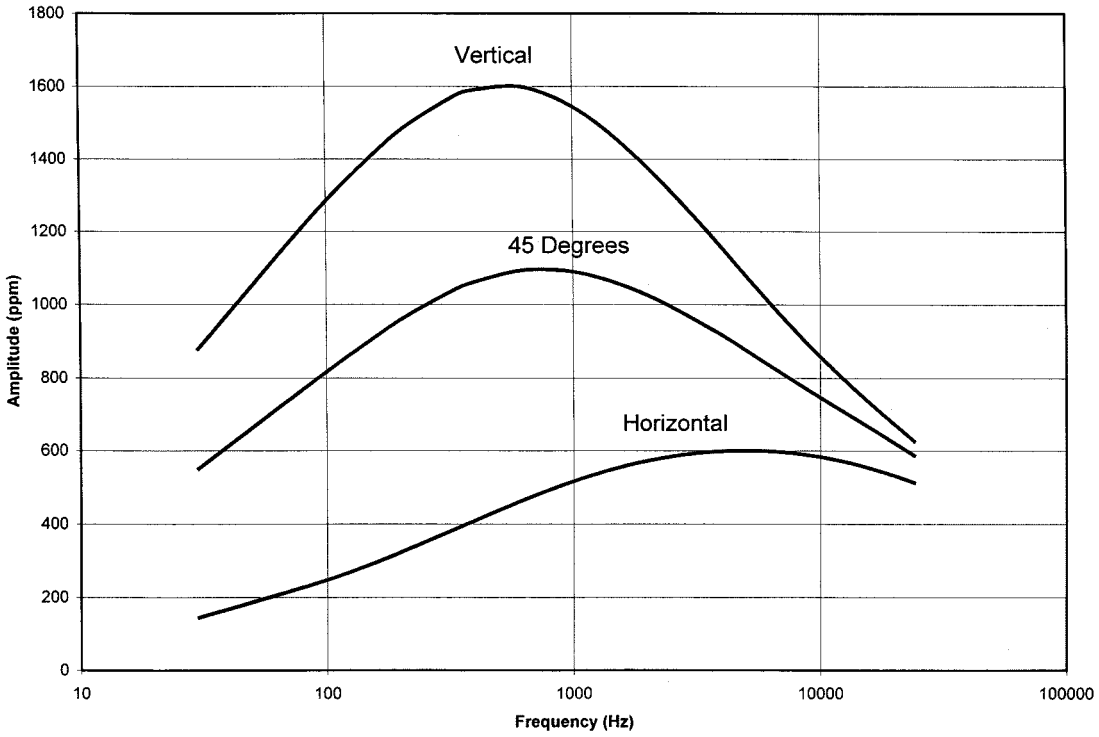

Fig. 1. Three curves are the quadrature responses of the GEM-3 sensor to a steel cylinder at three different orientations: vertical, 45°, and horizontal. Note that the frequency at which the peak occurs depends on the orientation of the cylinder. The measurements were made at one position of the sensor directly above the cylinder.

sampled data using a method to be explained shortly. The matrix $\boldsymbol{S}$ may be written

$$\boldsymbol{S} = \begin{pmatrix} s_{11} & s_{12} & s_{13} \\ s_{21} & s_{22} & s_{23} \\ s_{31} & s_{32} & s_{33} \end{pmatrix}. \tag{6}$$

This matrix is complex and symmetric, as reciprocity arguments demonstrate, so that six independent (complex) matrix elements define it. As a result, six inphase and quadrature observations performed at six different angles of incidence (i.e., corresponding to six different unit vectors $\boldsymbol{n}$) are sufficient to recover these elements and hence, $\boldsymbol{S}$. In general, more than six spatial measurements are desirable and the elements of $\boldsymbol{S}$ may be estimated by least squares. The next step is to compute the eigenvalues of $\boldsymbol{S}$ denoted by $\lambda_1(\omega)$, $\lambda_2(\omega)$, and $\lambda_3(\omega)$ for all excitation frequencies ω. Thus, diagonalizing $\boldsymbol{S}$ gives

$$\boldsymbol{S}(\omega) = \boldsymbol{O} \wedge (\omega) \boldsymbol{O}^{\tau} \tag{7}$$

where $\boldsymbol{O}$ is a rotation matrix, and

$$\wedge(\omega) = \begin{pmatrix} \lambda_1(\omega) & 0 & 0 \\ 0 & \lambda_2(\omega) & 0 \\ 0 & 0 & \lambda_3(\omega) \end{pmatrix}. \tag{8}$$

The (complex) eigenvalues $\lambda_1(\omega)$ characterize the target and are independent of orientation; these eigenvalues thus serve as our intrinsic target signatures when measured over a range of frequencies.

We note that nearly all ordnance are axially symmetric, or nearly so, which implies that $\lambda_1(\omega) \approx \lambda_2(\omega)$ if we choose the third axis as the symmetry axis. Thus, a general test for an object to be "ordnance-like" will be equality (or near equality) of two of its eigenvalues, which should differ significantly from the third eigenvalue for objects with a large aspect ratio.

To describe the procedure for computing the elements of the matrix $\boldsymbol{S}$ from data, we employ the following dyadic expansion of $\boldsymbol{S}$:

$$\boldsymbol{S} = \sum_{i=1}^{3}\sum_{j=1}^{3} s_{ij} \boldsymbol{x}_i \boldsymbol{x}_j \tag{9}$$

where $\boldsymbol{x}_1$, $\boldsymbol{x}_2$, and $\boldsymbol{x}_3$ are any set of convenient orthogonal unit vectors. As noted, because $s_{ij} = s_{ji}$, $\boldsymbol{S}$ is defined by the six independent elements $\{s_{11}, s_{22}, s_{33}, s_{12}, s_{13}, s_{23}\}$.

Suppose N measurements are made above ground, denoted by $emf_k^{(k)}$, with corresponding unit vectors $\boldsymbol{n}_k$, $k = 1, \ldots, N$. We then obtain by substituting (9) into (4), the following N equations in the six unknowns $\{s_{11}, s_{22}, s_{33}, s_{12}, s_{13}, s_{23}\}$:

$$emf_R^k = \sum_{i=1}^{3}\sum_{j=1}^{3} s_{ij} K_{ij}^k \, , k = 1, \ldots, N \tag{10}$$

where

$$K_{ij}^k \equiv (\boldsymbol{n}_k \cdot \boldsymbol{x}_i)(\boldsymbol{n}_k \cdot \boldsymbol{x}_j). \tag{11}$$

The N linear equations defined by (10) can then be solved to recover the six elements $\{s_{11}, s_{22}, s_{33}, s_{12}, s_{13}, s_{23}\}$. If N is greater than six, the resultant overdetermined system can be solved for the elements by the method of least squares. We solve

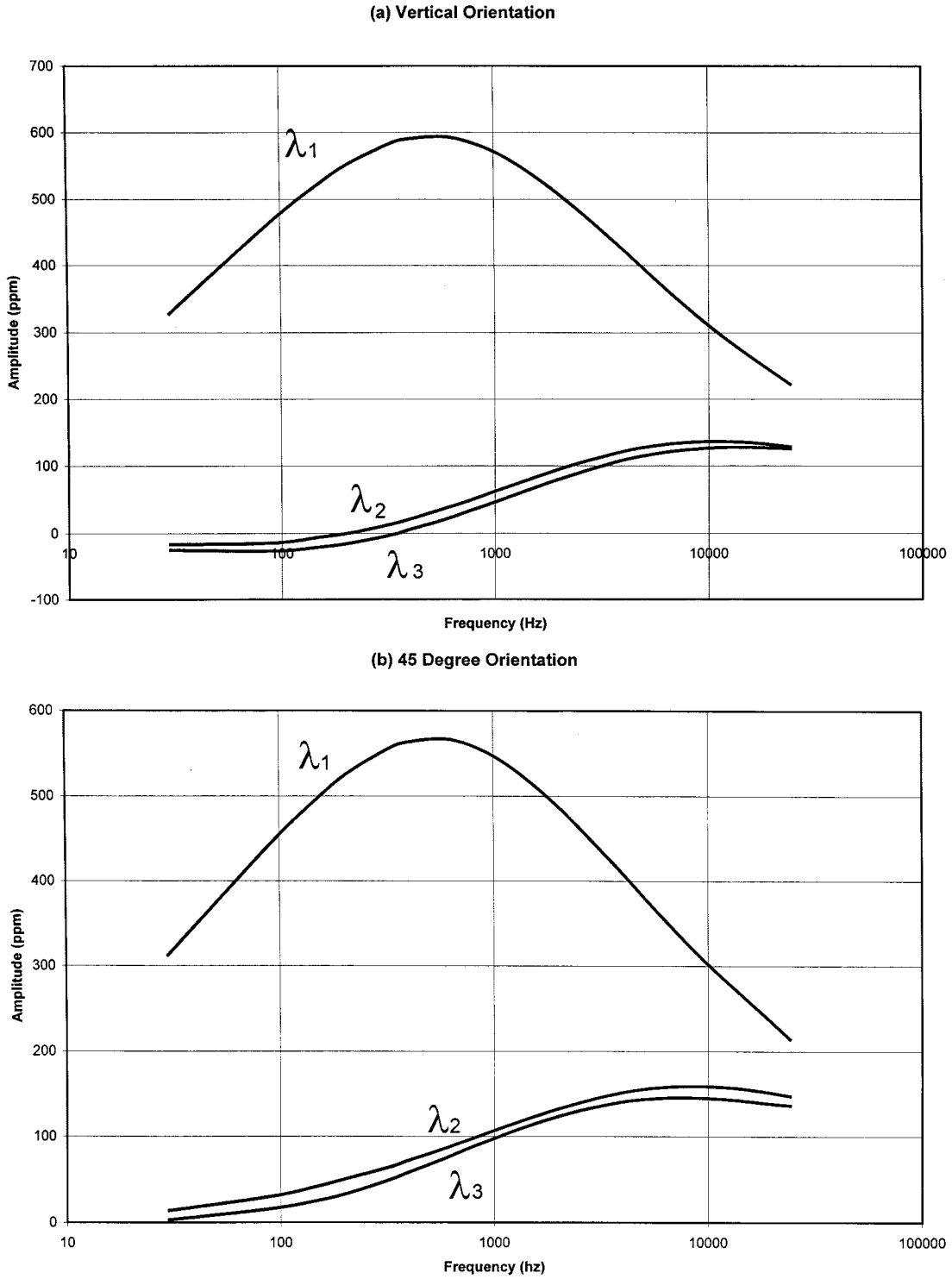

Fig. 2. These curves are the imaginary part (or quadrature component) of the eigenvalues derived from the steel cylinder plotted as a function of frequency. (a) and (b) Results derived from the cylinder in three orientations (vertical, 45°, and horizontal, respectively). In each case, the two transverse eigenvalue spectra are close together, reflecting the symmetry of the target.

the overdetermined system by computing its singular-value decomposition, which provides a quantitative measure of the "observability" of the matrix elements given a set of sensor coordinates that define the coefficients $K_{ij}^{(k)}$. Such a sensitivity analysis can be used to optimize the spatial sampling of sensor data to provide the most robust estimate of the elements of S. Ideally, we would like to position the sensor so that the incident magnetic field "views" the ordnance from many different directions.

Once the eigenvalues of S are computed and normalized in a manner to be described, the resulting orientation-independent signatures can then be compared to a set of precomputed library signatures, as explained next.

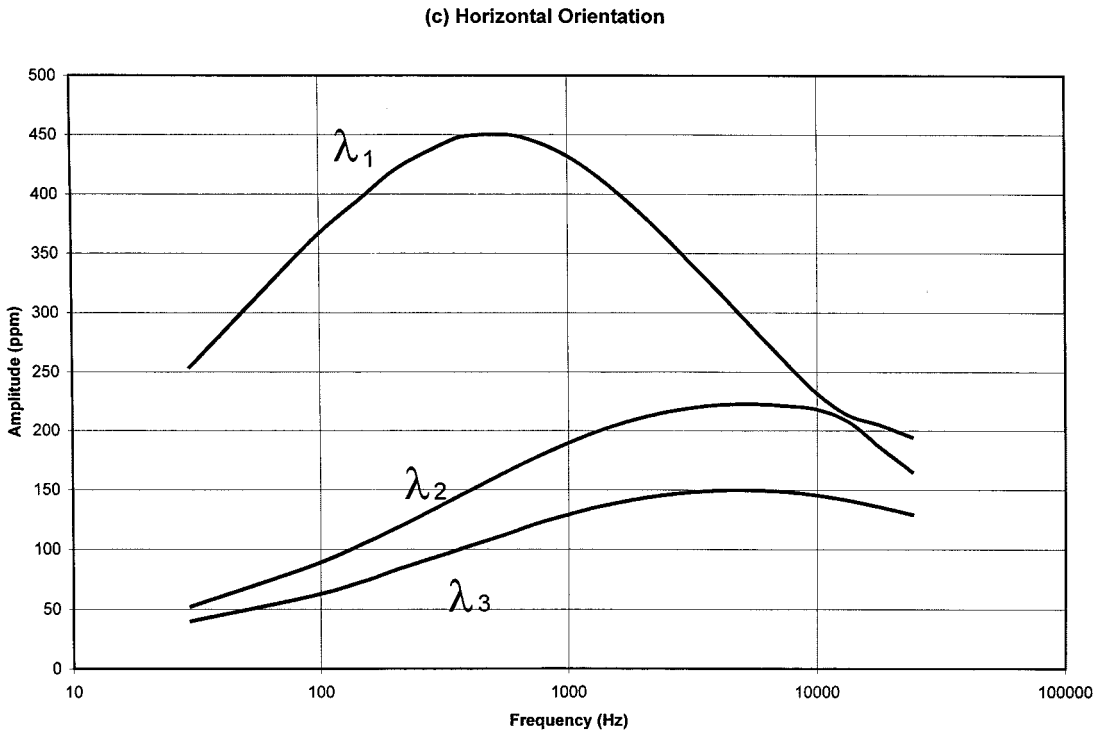

Fig. 2. *(Continued.)* These curves are the imaginary part (or quadrature component) of the eigenvalues derived from the steel cylinder plotted as a function of frequency. (c) Results derived from the cylinder in three orientations (vertical, 45°, and horizontal, respectively). In each case, the two transverse eigenvalue spectra are close together, reflecting the symmetry of the target.

IV. Depth Normalization and Library Fitting

A general procedure for selecting the best candidate signature is based on a likelihood ratio test. Let H denote the hypothesis that no UXO is present and H_n the hypothesis that the n-th UXO type is present; we then select the UXO that yields the largest ratio

$$\wedge_n(\lambda_1,\lambda_2,\lambda_3)=\frac{p(\lambda_1,\lambda_2,\lambda_3|H_n)}{p(\lambda_1,\lambda_2,\lambda_3|H_o)} \tag{12}$$

where $p(\lambda_1,\lambda_2,\lambda_3|H_n)$ is the conditional probability of observing $(\lambda_1,\lambda_2,\lambda_3)$ in the presence of the n-th UXO type. One can easily generalize the procedure to take into account *a priori* probabilities, e.g., if it is known that a certain UXO type is more prevalent than others at a given site. In the presence of Gaussian noise, the likelihood-ratio test reduces to finding the minimum mean-squared difference between a measured signature and a set of library signatures.

Let the data be recorded at M discrete frequencies ω_k and $k=1,\ldots,M$. Now, suppose that the buried UXO is of type n and denote by $\hat{\lambda}_i^{(n)}(\omega_k)$ the eigenvalues derived from the data and let $\lambda_i^{(m)}(\omega_k)$ denote the library eigenvalues associated with the m-th UXO type. The unknown object is then identified as the target that gives the smallest of the weighted mean-squared differences

$$E_m=\sum_{k=1}^{M}\sum_{i=1}^{3}W_k|\hat{\lambda}_i^{(n)}(\omega_k)-f\lambda_i^{(m)}(\omega_k)|^2 \tag{13}$$

where W_k is a positive weighting factor. In a maximum-likelihood (ML) interpretation, W_k may be regarded as inversely proportional to the variance of the data at frequency ω_k. In (13), f is the unknown amplitude scaling factor that appears in (5). As noted, we assume that f is independent of frequency. The ML estimate of f is obtained by minimizing E_m with respect to f . This can be obtained explicitly by setting $\partial E_m/\partial f=0$ and solving for f, giving

$$f=\frac{\mathrm{Re}\sum_{k=1}^{M}\sum_{i=1}^{3}W_k\hat{\lambda}_i^{(n)}(\omega_k)^*\lambda_i^{(m)}(\omega_k)}{\sum_{k=1}^{M}\sum_{i=1}^{3}W_k|\lambda_i^{(m)}(\omega_k)|^2} \tag{14}$$

where Re means real part. When this expression for f is inserted back into (13), the mean-square error (MSE) E_m will vanish when $m=n$, as desired. We remark that the value of f could be used to determine target depth once the target has been identified and assuming that a calibration procedure can be carried out for each possible target. A plot of f versus depth will then give the target depth relative to the library target depth. For example, when $f=1$, the target and the library target are at the same depth, and when $f<1$, the target is deeper than the library target, and so on.

In (13), it is implicitly assumed that the scaling factor f is identical for the real and imaginary parts of all three eigenvalues; this assumption holds in theory in the limit of a uniform incident field. In practice, better results are obtained by computing six scaling factors, one each for the real and imaginary parts of all three eigenvalues, which we denote by $f_{R,i}$ and $f_{I,i}$, where $i=1,2,3,$. In other words, letting $\lambda_{R,i}$ and $\lambda_{I,i}$ denote the real and imaginary parts of λ_i, we rewrite (13) as

$$E_m=\sum_{k=1}^{M}\sum_{i=1}^{3}W_k\left\{[\hat{\lambda}_{R,i}^{(n)}(\omega_k)-f_{R,j}\lambda_{R,i}^{(m)}(\omega_k)]^2 +[\hat{\lambda}_{I,i}^{(n)}(\omega_k)-f_{I,i}\lambda_{I,i}^{(m)}(\omega_k)]^2\right\}. \tag{15}$$

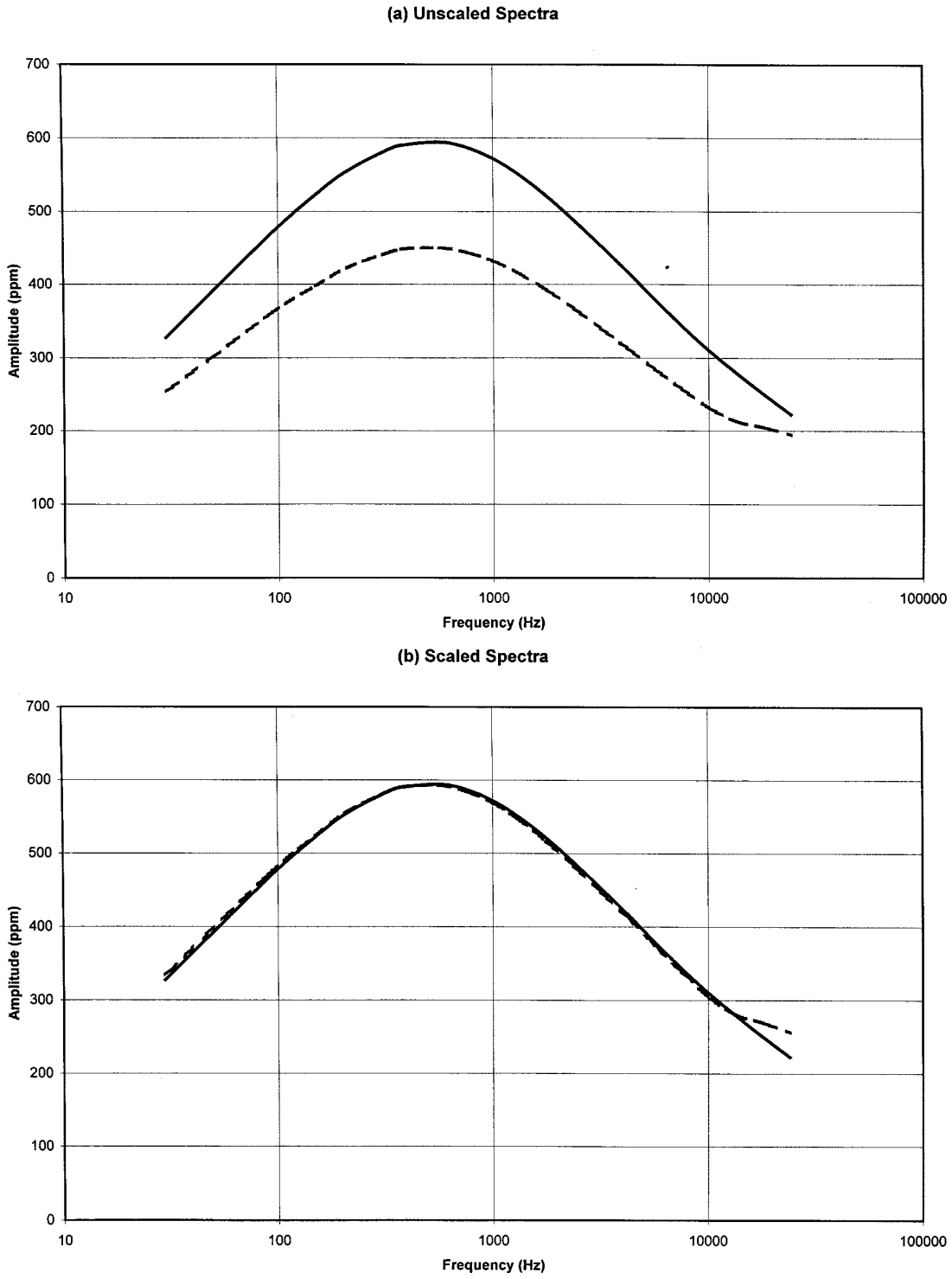

Fig. 3. The figure illustrates the normalization procedure applied to the spectra before the MSE is computed. The lower curve in (a) is multiplied by an optimally derived scale factor so that it matches the upper curve, as shown in (b).

The scale factors that follow from this expression are

$$f_{R,i} = \frac{\sum_{k=1}^{M} W_k \hat{\lambda}_{R,i}^{(n)}(\omega_k) \lambda_{R,i}^{(m)}(\omega_k)}{\sum_{k=1}^{M} W_k \lambda_{R,i}^{(m)}(\omega_k)^2} \tag{16}$$

where $i = 1, 2, 3$, and a similar expression can be written for $f_{I,i}$.

V. Experiments With Cylinders

To demonstrate the above theory, the GEM-3 sensor was used to record multifrequency data over aluminum, brass, and ferrous steel cylinders. The cylinders were the same size and shape: 3.2 cm in diameter and 7.6 cm long. The center of the sensor head was moved relative to the center of the cylinder on a 7×7 square grid of points. The grid point separation was 10 cm. The distance

between the plane of the grid and the center of the cylinder was 20 cm (the "depth"). For each cylinder type (aluminum, brass, steel), data were taken at three orientations of the cylinder: vertical, horizontal and 45° from vertical. This set of measurements was first performed in free space (away from the ground) and again with the cylinders buried in the ground to determine the effects of the conductivity and permeability of the earth on the measurements. Thus, a total of 18 measurements where performed, each at 12 frequencies. The frequencies were 30, 90, 150, 210, 330, 390, 570, 750, 990, 1290, 1770, and 2370 Hz. These measurements are summarized in Table I.

A. Orientation Invariants

Fig. 1 shows the quadrature component of the spectral data recorded with the sensor directly over the steel cylinder at the three different orientations of the cylinder. Note that the peak of the quadrature shifts with the orientation of the cylinder. This orientation dependence exemplifies the need for a pre-processing step to extract invariant signatures before a meaningful comparison to a set of library signatures can be made.

Fig. 2(a)–(c) show the quadrature spectra (or imaginary part) of the three eigenvalues of the steel cylinder derived using the theory of Section III. These results were computed using the entire grid of data. The analysis was repeated for all three orientations of the cylinder. In theory, the results should be independent of orientation, that is, Figs. 2(a)–(c) should look identical. Except for some differences in amplitude, the shapes of the curves are very similar, with the peaks of the corresponding curves occurring at frequencies essentially independent of orientation. Also, as expected, two of the eigenvalue spectra nearly coincide, reflecting the fact that two of the eigenvalues are degenerate due to the axial symmetry of the cylinder. These two eigenvalues correspond to the two transverse principal axes, whereas the upper curve corresponds to the longitudinal axis of the cylinder.

These three figures demonstrate that the orientation dependence, clearly apparent in Fig. 1, has been removed by the eigendecomposition. The differences in amplitudes between corresponding curves in Fig. 2(a)–(c) are probably due to the finite size of the cylinders. For example, the near end of the vertical cylinder is closer to the sensor head than any part of the horizontal cylinder. The larger separation of the transverse eigenvalues in Fig. 2(c) compared to Fig. 2(a) and 2(b) is probably due to noise, since the horizontal orientation gives the weakest signal.

B. Scale Normalization

As an illustration of the normalization procedure outlined in Section IV, consider the problem of scaling the two longitudinal eigenvalue spectra (upper curves) shown in Fig. 2(a) and 2(c) to make them coincide. The two curves are plotted together in Fig. 3(a). Here, we arbitrarily let the lower curve play the role of the library signature. After multiplying the lower curve by the scaling factor $f = 1.317$ computed from (16), we see that they now essentially coincide, as shown in Fig. 3(b). To perform library matching, we compute all six scale factors for the eigenvalues $\lambda_{R,i}$ and $\lambda_{I,i}$, and $i = 1, 2, 3,$, and substitute these into (15).

TABLE II
GOODNESS-OF-FIT VALUES COMPUTED FROM (15) FOR CYLINDERS

	Library: Aluminum	Library: Brass	Library: Steel
Aluminum V	.0000	.1093	.8907
Aluminum H	.0001	.1136	.8863
Aluminum 45	.0001	.1053	.8946
Aluminum V (G)	.0222	.0527	.9250
Aluminum H (G)	.0036	.0927	.9037
Aluminum 45 (G)	.0112	.0732	.9156
Brass V	.1018	.0000	.8982
Brass H	.1071	.0002	.8927
Brass 45	.1124	.0005	.8871
Brass V (G)	.1905	.0250	.7845
Brass H (G)	.1430	.0066	.8504
Brass 45 (G)	.1509	.0078	.8414
Steel V	.5036	.4964	.0000
Steel H	.5058	.4914	.0027
Steel 45	.6541	.3106	.0353
Steel V (G)	.4670	.4969	.0361
Steel H (G)	.5034	.4924	.0042
Steel 45 (G)	.6643	.3169	.0188

TABLE III
UXO TYPES

20 mm projectile	Diameter: 2.0 cm	Length: 7.3 cm
30 mm projectile	Diameter: 3.0 cm	Length: 10.7 cm
37 mm projectile	Diameter: 3.7 cm	Length: 10.9 cm
41 mm projectile	Diameter: 4.1 cm	Length: 8.0 cm

C. Matching to Library Signatures

To illustrate the matching procedure, we took the data labeled 1, 7, and 13 in Table I to serve as our library data. After the eigenvalue decomposition and the scale factors were calculated, the MSE was computed between the library signatures and all of the data by evaluating (15). Note, of course, that cases 1, 7, and 13 should result in zero error, since these play the role of library data, but the remaining 15 cases will give nonzero error. Our objective is to see whether, for these 15 cases, the cylinders made of the different metals are properly matched, independently of orientation and scaling errors. The results of this exercise are given in Table II, where the MSEs are listed. In this table, V, H and 45 denote data acquired from cylinders oriented vertically, horizontally and at 45°. The label (G) refers to measurements of cylinders in the ground.

We performed the MSE computation using all three eigenvalues, λ_i, $i = 1, 2, 3$, and again using only the largest eigenvalue (λ) corresponding to the upper curves in Fig. 2. For this set of targets, the latter case gave somewhat larger differences in the MSEs and these results are listed in Table II. Ide-

TABLE IV
UXO DATA

1.	20 mm projectile	Vertical	Free space
2.	20 mm projectile	Horizontal	Free space
3.	20 mm projectile	45 Degrees	Free space
4.	30 mm projectile	Vertical	Free space
5.	30 mm projectile	Horizontal	Free space
6.	30 mm projectile	45 Degrees	Free space
7.	37 mm projectile	Vertical	Free space
8.	37 mm projectile	Horizontal	Free space
9.	37 mm projectile	45 Degrees	Free space
10.	41 mm projectile	Vertical	Free space
11.	41 mm projectile	Horizontal	Free space
12.	41 mm projectile	45 Degrees	Free space

TABLE V
GOODNESS-OF-FIT VALUES COMPUTED FROM (15) FOR FOUR UXO TYPES

	Library: 20 mm projectile	Library: 41 mm projectile	Library: 30 mm projectile	Library: 37 mm projectile
20 mm projectile V	.0263	.7749	.0919	.1070
20 mm projectile 45	.0652	.5632	.1696	.2020
20 mm projectile H	.0259	.7966	.0914	.0861
41 mm projectile V	.3151	.0026	.3594	.3229
41 mm projectile 45	.3151	.0043	.3575	.3231
41 mm projectile H	.3152	.0035	.3581	.3231
30 mm projectile V	.0438	.9107	.0009	.0446
30 mm projectile 45	.0278	.9033	.0070	.0619
30 mm projectile H	.0263	.9067	.0243	.0427
37 mm projectile V	.0498	.8932	.0543	.0027
37 mm projectile 45	.0629	.8597	.0769	.0005
37 mm projectile H	.0629	.8562	.0782	.0028

ally, the columns and rows labeled "Aluminum" should give a small MSE, and so on. This is seen to be the case.

VI. EXPERIMENTS WITH UXO

The same procedure applied to the cylinder data and described in the previous section was performed on four types of UXO (Table III). The UXO are made predominantly of ferrous steel. A set of "test data" were recorded by measuring the response of each UXO type over a 5×5 grid in free space. The grid point spacing was 10 cm and the distance between the plane of the grid and the center of the UXO was 25 cm (the "depth"). For each UXO type, measurements were again recorded at three orientations: vertical, horizontal and 45° (summarized in Table IV and denoted by "V", "H," and "45"). Measurements were made at ten frequencies (30, 90, 150, 270, 570, 1230, 2610, 5430, 11430, 20 070 Hz). Library data were recorded over the 5×5 grid at the same set of frequencies but at the slightly larger "depth" of 35 cm. The library data were derived from each UXO type oriented in the vertical direction only. The fitting procedure was carried out by computing (15) and (16), and the resulting goodness-of-fit values computed from (15) are listed in Table V. We see from the table that the UXO are correctly identified independently of orientation. Again, "correct identification" occurs when the true target results in the smallest least-squared error.

VII. CONCLUSION

Broadband electromagnetic induction (EMI) data have been previously shown to be effective in identifying different UXO types and in discriminating UXO from clutter. However, the orientation and depth dependence of the sensor response needs to be accounted for before unknown and library signatures can be meaningfully compared. Here, we describe a procedure based on comparing the depth-normalized (scaled) eigenvalues of the target's magnetic polarizability tensor. The procedure is linear and noniterative. The theory is based on a dipole model given by (1), which represents the lowest order term in a multipole expansion of the target response. The theory is demonstrated here with measurements made from cylinders and UXO.

REFERENCES

[1] I. J. Won, D. A. Keiswetter, G. R. A. Fields, and L. C. Sutton, "Gem-2: A new multifrequency electomagnetic sensor," *J. Environ. Eng. Geophys.*, vol. 1, pp. 129–137, 1996.
[2] I. J. Won, D. A. Keiswetter, D. R. Hanson, E. Novikova, and T. M. Hall, "Gem-3: A monostatic broadband electromagnetic induction sensor," *J. Environ. Eng. Geophys.*, vol. 2, pp. 53–64, 1997.
[3] I. J. Won, D. A. Keiswetter, and E. Novikova, "Electromagnetic induction spectroscopy," *J. Environ. Eng. Geophys.*, vol. 3, pp. 27–40, 1998.
[4] T. H. Bell, B. Barrow, and N. Khadr, "Shape-based classification and discrimination of subsurface objects using electromagnetic induction," in *Proc. Int. Geoscience and Remote Sensing Symp. (IGARSS)*, Seattle, WA, July 6–10, 1998.
[5] B. J. Barrow and H. H. Nelson, "Model-based characterization of EM induction signatures for UXO/clutter discrimination using the MTADS platform," in *Proc. UXO Forum*, Atlanta, GA, May 25–27, 1999.
[6] M. Ozdemir, E. L. Miller, and S. J. Norton, "Localization and characterization of buried objects from multi-frequency, array inductive data," in *Proc. SPIE*, Orlando, FL, 1998.
[7] Y. Das, J. E. McFee, J. Toews, and G. C. Stuart, "Analysis of an electromagnetic induction detector for real-time location of buried objects," *IEEE Trans. Geosci. Remote Sensing*, vol. 28, pp. 278–288, Mar. 1990.
[8] C. E. Baum, Ed., *Detection and Identification of Visually Obscured Targets*. Philadelphia, PA: Taylor and Frances, 1999.
[9] M. L. Burrows, "A theory of eddy-current flaw detection," Ph.D. dissertation, Univ. Michigan, Ann Arbor, 1964.

Stephen J. Norton received the B.A. degree in physics from the University of California, Berkeley, in 1971, and the Ph.D. degree in applied physics from Stanford University, Stanford, in 1976.

From 1977 to 1979, he was a National Research Council Postdoctoral Fellow with the National Bureau of Standards and from 1979 to 1993, he was with the National Institute of Standards and Technology, Gaithersburg, MD, working in the fields of medical imaging and the nondestructive evaluation of materials. He then spent five years at the Oak Ridge National Laboratory, Oak Ridge, TN, working in the area of geophysical imaging before joining Geophex, Ltd., Raleigh, NC, in 1998. He has published about 75 papers on all aspects of inversion and imaging, including diffraction tomography, magnetic resonance imaging, Mossbauer tomography, ultrasonic imaging in medicine and NDE, Compton scattering tomography, and EMI imaging.

I. J. Won received the B.S. degree in mining and petroleum engineering from the Seoul National University, Seoul, Korea, in 1967, and the M.S. and Ph.D. degree in geophysics from Columbia University, New York, in 1971 and 1973, respectively.

He is currently Technical Director and President of Geophex, Ltd., Raleigh, NC, an independent geological and environmental consulting firm he founded in 1983. From 1976 to 1989, he was an Assistant Professor, Associate Professor, and Professor of geophysics at North Carolina State University, Raleigh. He has published over 80 research and review articles in refereed technical journals and books.